



Two Lensed Star Candidates at $z \simeq 4.8$ behind the Galaxy Cluster MACS J0647.7+7015

Ashish Kumar Meena¹ , Adi Zitrin¹ , Yolanda Jiménez-Teja^{2,3} , Erik Zackrisson⁴ , Wenlei Chen⁵ , Dan Coe^{6,7,8} , Jose M. Diego⁹ , Paola Dimauro¹⁰ , Lukas J. Furtak¹ , Patrick L. Kelly⁵ , Masamune Oguri^{11,12} , Brian Welch^{13,14,15} , Abdurro'uf^{6,8} , Felipe Andrade-Santos^{16,17} , Angela Adamo¹⁸ , Rachana Bhatawdekar¹⁹ , Maruša Bradac^{20,21} , Larry D. Bradley⁶ , Tom Broadhurst^{22,23,24} , Christopher J. Conselice²⁵ , Pratika Dayal²⁶ , Megan Donahue²⁷ , Brenda L. Frye²⁸ , Seiji Fujimoto^{29,35} , Tiger Yu-Yang Hsiao⁸ , Vasily Kokorev³⁰ , Guillaume Mahler^{31,32} , Eros Vanzella³³ , and Rogier A. Windhorst³⁴

¹ Physics Department, Ben-Gurion University of the Negev, P.O. Box 653, Be'er-Sheva 84105, Israel; ashishmeena766@gmail.com

² Instituto de Astrofísica de Andalucía, Glorieta de la Astronomía s/n, E-18008 Granada, Spain

³ Observatório Nacional—MCTI (ON), Rua Gal. José Cristiano 77, São Cristóvão, 20921-400, Rio de Janeiro, Brazil

⁴ Observational Astrophysics, Department of Physics and Astronomy, Uppsala University, Box 516, SE-751 20 Uppsala, Sweden

⁵ School of Physics and Astronomy, University of Minnesota, 116 Church Street SE, Minneapolis, MN, 55455, USA

⁶ Space Telescope Science Institute (STScI), 3700 San Martin Drive, Baltimore, MD, 21218, USA

⁷ Association of Universities for Research in Astronomy (AURA) for the European Space Agency (ESA), STScI, Baltimore, MD, USA

⁸ Center for Astrophysical Sciences, Department of Physics and Astronomy, The Johns Hopkins University, 3400 N Charles St. Baltimore, MD, 21218, USA

⁹ Instituto de Física de Cantabria (CSIC-UC). Avda. Los Castros s/n. E-39005 Santander, Spain

¹⁰ INAF—Osservatorio Astronomico di Roma, via di Frascati 33, I-00078 Monte Porzio Catone, Italy

¹¹ Center for Frontier Science, Chiba University, 1-33 Yayoi-cho, Inage-ku, Chiba 263-8522, Japan

¹² Department of Physics, Graduate School of Science, Chiba University, 1-33 Yayoi-cho, Inage-Ku, Chiba 263-8522, Japan

¹³ Department of Astronomy, University of Maryland, College Park, MD, 20742, USA

¹⁴ Observational Cosmology Lab, NASA Goddard Space Flight Center, Greenbelt, MD, 20771, USA

¹⁵ Center for Research and Exploration in Space Science and Technology, NASA/GSFC, Greenbelt, MD, 20771, USA

¹⁶ Department of Liberal Arts and Sciences, Berklee College of Music, 7 Haviland Street, Boston, MA, 02215, USA

¹⁷ Center for Astrophysics Harvard & Smithsonian, 60 Garden Street, Cambridge, MA, 02138, USA

¹⁸ Department of Astronomy, Oskar Klein Centre, Stockholm University, AlbaNova University Centre, SE-106 91 Stockholm, Sweden

¹⁹ European Space Agency, ESA/ESTEC, Keplerlaan 1, 2201 AZ Noordwijk, The Netherlands

²⁰ Department of Mathematics and Physics, University of Ljubljana, Jadranska ulica 19, SI-1000 Ljubljana, Slovenia

²¹ Department of Physics and Astronomy, University of California, Davis, 1 Shields Ave, Davis, CA, 95616, USA

²² Department of Theoretical Physics, University of the Basque Country UPV/EHU, Bilbao, Spain

²³ Donostia International Physics Center (DIPC), E-20018 Donostia, Spain

²⁴ IKERBASQUE, Basque Foundation for Science, Bilbao, Spain

²⁵ Jodrell Bank Centre for Astrophysics, University of Manchester, Oxford Road, Manchester, UK

²⁶ Kapteyn Astronomical Institute, University of Groningen, P.O. Box 800, 9700 AV Groningen, The Netherlands

²⁷ Michigan State University, Physics & Astronomy Department, East Lansing, MI, USA

²⁸ Department of Astronomy/Steward Observatory, University of Arizona, 933 N. Cherry Avenue, Tucson, AZ, 85721, USA

²⁹ Department of Astronomy, The University of Texas at Austin, Austin, TX, 78712, USA

³⁰ Kapteyn Astronomical Institute, University of Groningen, PO Box 800, 9700 AV Groningen, The Netherlands

³¹ Centre for Extragalactic Astronomy, Durham University, South Road, Durham, DH1 3LE, UK

³² Institute for Computational Cosmology, Durham University, South Road, Durham, DH1 3LE, UK

³³ INAF—OAS, Osservatorio di Astrofisica e Scienza dello Spazio di Bologna, via Gobetti 93/3, I-40129 Bologna, Italy

³⁴ School of Earth and Space Exploration, Arizona State University, Tempe, AZ, 85287-1404, USA

Received 2022 December 3; revised 2023 January 7; accepted 2023 January 7; published 2023 February 9

Abstract

We report the discovery of two extremely magnified lensed star candidates behind the galaxy cluster MACS J0647.7+015 using recent multiband James Webb Space Telescope (JWST) NIRCам observations. The star candidates are seen in a previously known, $z_{\text{phot}} \simeq 4.8$ dropout giant arc that straddles the critical curve. The candidates lie near the expected critical curve position, but lack clear counter-images on the other side of it, suggesting these are possibly stars undergoing caustic crossings. We present revised lensing models for the cluster, including multiply imaged galaxies newly identified in the JWST data, and use them to estimate background macro-magnifications of at least $\gtrsim 90$ and $\gtrsim 50$ at the positions of the two candidates, respectively. With these values, we expect effective, caustic-crossing magnifications of $\sim [10^3 - 10^5]$ for the two star candidates. The spectral energy distributions of the two candidates match well the spectra of B-type stars with best-fit surface temperatures of $\sim 10,000$ K, and $\sim 12,000$ K, respectively, and we show that such stars with masses $\gtrsim 20 M_{\odot}$ and $\gtrsim 50 M_{\odot}$, respectively, can become sufficiently magnified to be observable. We briefly discuss other alternative explanations and conclude that these objects are likely lensed stars, but also acknowledge that the less-magnified candidate may alternatively reside in a star cluster. These star candidates constitute the second highest-redshift examples to date after Earendel at $z_{\text{phot}} \simeq 6.2$, establishing further the potential of studying extremely magnified stars at high

³⁵ Hubble Fellow.

redshifts with JWST. Planned future observations, including with NIRSpec, will enable a more detailed view of these candidates in the near future.

Unified Astronomy Thesaurus concepts: [Strong gravitational lensing \(1643\)](#); [Gravitational microlensing \(672\)](#); [Massive stars \(732\)](#)

1. Introduction

The serendipitous discovery by Kelly et al. (2018) several years ago of the first highly magnified star in Hubble Space Telescope (HST) imaging in the MACS J1149.5+2223 galaxy cluster ($z = 0.544$; Ebeling et al. 2007), has opened a new window to observe stars at cosmological distances (e.g., Miralda-Escude 1991). The star (named ‘‘Icarus’’; Kelly et al. 2018) was detected in a strongly lensed spiral galaxy ($z = 1.49$) and was found to have an estimated magnification factor of ~ 2000 . Several other lensed stars were since detected in HST imaging in various galaxy clusters (Rodney et al. 2018; Chen et al. 2019; Kaurov et al. 2019; Diego et al. 2022a; Meena et al. 2022b; Welch et al. 2022a), with rapidly increasing numbers (Kelly et al. 2022). Thanks to the larger photon collecting area compared to HST, and its sensitivity to infrared light, the James Webb Space Telescope (JWST; Gardner et al. 2006) significantly enhances our ability to detect such lensed stars, especially at higher redshifts (Windhorst et al. 2018; Meena et al. 2022a). So far, nearly all galaxy clusters observed by JWST have revealed lensed stars (Chen et al. 2022; Diego et al. 2022b; Pascale et al. 2022; Welch et al. 2022b; and several more are forthcoming), showcasing the promising rate of such detections.

Observing highly magnified stars at cosmological distances is typically the result of a combined effect of strong- and microlensing (e.g., Miralda-Escude 1991; Oguri et al. 2018). The presence of point-like masses (such as stellar-mass objects) in the lens leads to the formation of microcritical curves and microcaustics in the lens and source planes, respectively. The area covered by each of these microcritical curves depends on the perturber’s mass and on the macro-magnification (the higher the mass and macro-magnification, the larger the area) and at sufficiently high macro-magnifications the microcritical curves merge with each other to form a corrugated network (e.g., Venumadhav et al. 2017; Diego 2018; Diego et al. 2018). Whenever a compact source, such as, e.g., a star in a strongly lensed galaxy, crosses a microcaustic, it gets highly magnified, leading to a peak in its light curve, which might make it observable for a brief period of time as a transient source. The height, width, and frequency of these peaks depend on various factors such as the relative velocity and radius of the source, the surface densities of the microlenses, and their mass function (e.g., Venumadhav et al. 2017). If the underlying magnification is sufficiently high, and the corrugated microcaustic network is dense enough, highly magnified stars may be seen as persistent sources with only moderate fluctuations (e.g., Welch et al. 2022a, 2022b).

The substantial magnification provided by galaxy cluster lenses has also continuously led to the detection of background high-redshift galaxy candidates in observations with the HST (e.g., Coe et al. 2013; Chan et al. 2017; Salmon et al. 2018; Bhatavdekar et al. 2019) and JWST (e.g., Adams et al. 2022; Atek et al. 2022; Castellano et al. 2022; Furtak et al. 2022; Hsiao & Coe 2022; Vanzella et al. 2022; Williams et al. 2022; Yan et al. 2022). One of these candidates is MACS0647-JD (Coe et al. 2013), a record-breaking, triply imaged galaxy

at $z \simeq 10.7$, which was first detected in HST imaging of the MACS J0647.7+7015 (hereafter MACS0647; $z = 0.591$, Ebeling et al. 2007) galaxy cluster under the Cluster Lensing and Supernova survey with Hubble (CLASH)³⁶ program (Postman et al. 2012). To study MACS0647-JD in more detail, the JWST general observer (GO) program 1433 (PI: Dan Coe) targeted the cluster and obtained JWST/NIRCam imaging in six different filters. The JWST imaging supported the high-redshift nature at $z_{\text{phot}} = 10.6$ with very high confidence, and revealed that MACS0647-JD is actually made of two components separated by a distance of ~ 400 pc, and a possible third clump about 3 kpc away (Hsiao & Coe 2022).

In this work, we present and study the properties of two extremely magnified lensed star candidates identified in these JWST/NIRCam observations of MACS0647. The candidates are seen in a giant arc at a redshift of $z_{\text{phot}} = 4.79^{+0.07}_{-0.15}$ lensed by the cluster. They are identified primarily by their compactness, their position in the arc, and their proximity to the critical curve (implying very high background magnifications), and a lack of counter-images (implying they are possibly experiencing a local temporary extreme magnification, or alternatively sit sufficiently close to the macro-caustic so that their two counter-images are merged into a single unresolved image).

This paper is organized as follows: in Section 2, we briefly describe the JWST/NIRCam imaging of MACS0647. In Section 3, we present a revised strong lens models for MACS0647, needed for interpretation of the sources. In Section 4, we discuss the highly magnified lensed star candidates. The cosmological parameters used in this work to estimate the various parameters are $H_0 = 70 \text{ km s}^{-1} \text{ Mpc}^{-1}$, $\Omega_m = 0.3$, and $\Omega_\Lambda = 0.7$. With these, $1''$ corresponds to 6.37 kpc at the cluster redshift. All magnitudes are in the AB system (Oke & Gunn 1983).

2. JWST Data

MACS0647 was observed by JWST in 2022 September as part of a cycle 1 GO program (program ID: 1433; PI: Dan Coe). All of the corresponding data products are publicly available on the Mikulski Archive for Space Telescopes (MAST) website at the Space Telescope Science Institute. The specific observations analysed can be accessed via [10.17909/d2er-wq71](https://doi.org/10.17909/d2er-wq71). Within this program, MACS0647 was observed in six NIRCam filters, F115W, F150W, F200W, F277W, F356W, and F444W, spanning the wavelength range from ~ 1 to $\sim 5 \mu\text{m}$.³⁷ In each filter, the total exposure time was 2104 s, reaching a 5σ limiting magnitude in the range 28–29 AB. We note that additional imaging in F200W and F480M, along with NIRSpec spectroscopic observations, are expected to be conducted in early 2023 on this target.

In this work we use images reduced with the GRIZLI software (Brammer et al. 2022) and photometric redshifts estimated using EAZY (Brammer et al. 2008). In

³⁶ <https://www.stsci.edu/~postman/CLASH/>

³⁷ <https://s3.amazonaws.com/grizli-v2/JwstMosaics/v4/index.html>

addition to the JWST data, HST observations in 16 ACS and WFC3 filters covering UV to near-infrared wavelengths are also used, mainly from the CLASH program (GO 12101; PI: Postman), including previous data from GO 9722 (PI: Ebeling), GO 10493, 10793 (PI: Gal-Yam), and GO 13317 (PI: Coe) programs, (see Ebeling et al. 2007; Postman et al. 2012; Coe et al. 2013).

For more details about the data and their reduction procedure, we refer the reader to Hsiao & Coe (2022).

3. Strong Lens Modeling of MACS0647

Strong lens models for MACS0647 have been constructed in the past based on HST observations. The first preliminary lens model for MACS0647 was presented in Zitrin et al. (2011) based on two multiple-image systems found in pre-CLASH, HST/ACS F555W+F814W imaging, using the `Light-Trace-Mass` (LTM; Zitrin et al. 2009) method. In Coe et al. (2013) seven new multiple-image systems were identified in CLASH observations, including MACS0647-JD at $z \simeq 10.6$. Based on the previous and newly identified systems Coe et al. (2013) refined the previous LTM lens model and presented two additional lens models using `Lenstool` (parametric; Kneib et al. 1993; Jullo et al. 2007) and `LensPerfect` (nonparametric; Coe et al. 2008). Zitrin et al. (2015) identified three additional strongly lensed system candidates, bringing the total number of strongly lensed systems known in this cluster to 12 in pre-JWST observations. Furthermore, a `GlaFic` (Oguri 2010) lens model for MACS0647 was discussed in Okabe et al. (2020).

Thanks to its superior capabilities in (near-) infrared resolution and depth, JWST brings forth a large number of new lensed sources. We have visually inspected the JWST images and identified 11 new strongly lensed system candidates—and following similar symmetries—in addition to the 12 already known. A complete list of the 23 multiple-image systems is given here in Table 2. In addition to the newly identified lensed image candidates, we also detect multiple pairs of small-scale substructures within some of these lensed images. For example, system 6, according to the HST images was an isolated triply imaged galaxy. However, JWST imaging reveals that it consists of two clumps with a separation of ~ 400 pc from each other (Hsiao & Coe 2022). Similarly, in the giant lensed arc at $z \simeq 4.8$ (system 2), we observe multiple pairs of strongly lensed stellar clumps in the source (see Figure 3).

We here construct revised lens models for MACS0647 using our `dPIEeNFW` (see Zitrin et al. 2015) and `GlaFic` (Oguri 2010) codes. These new mass models are based on the earlier known multiple-image systems, as well as the newly found ones. To our knowledge, none of the multiple-image systems have a spectroscopic redshift measurement. However, the dropout nature of the $z \simeq 4.8$ arc and the JD object, for example, which also span a large range of lensing distance ratios, together with tightly constrained multiband-based (16 HST + 6 JWST) photometric redshifts for most systems, allow us to construct robust lens models.

Both of the lens models used here are parametric in nature. The `dPIEeNFW` implementation which we use is a revised version of the parametric code of Zitrin et al. (2015) used to map the CLASH sample and the Hubble Frontier Fields. The main improvement is that the new version is not grid-based and thus can reach higher resolutions and gives more accurate results. The new method has already been implemented on various clusters with JWST data (e.g.,

Roberts-Borsani et al. 2022; Hsiao & Coe 2022; Pascale et al. 2022; Williams et al. 2022).³⁸ Here we use 175 cluster members chosen by the red sequence of the cluster and parametrized as double pseudo-isothermal elliptical mass-density profiles, and two cluster-scale dark matter (DM) halos each parameterized as an elliptical Navarro–Frenk–White (NFW; Navarro et al. 1996) profile. The centers of these are optimized in the minimization procedure, around the positions of the central brightest cluster galaxies. Minimization is done in the source plane (Keeton 2010), via a several-dozen thousand step Markov Chain Monte Carlo (MCMC), from which the uncertainties are derived as well. The `GlaFic` modeling code (Oguri 2010) has been successfully applied to a large sample of clusters before, and was proven to be very robust when compared to numerically simulated clusters, or for time-delay predictions (e.g., Kelly et al. 2016; Meneghetti et al. 2017). Pseudo-Jaffe profiles are used to describe galaxies whereas the DM halos are described with elliptical NFW profiles.

The critical curves for a source at redshift 4.8 from the two models are shown in Figure 1. Due to many bright foreground stars, we also see the corresponding bright blue-green diffraction spikes around them. The green-colored linear features (known as “claws” and “Dragon’s Breath Type II”) near lensed images 5.1, 12.3, and 21.2, are artifacts caused by the presence of bright stars far from the field of view (also see Section 2.4 in Hsiao & Coe 2022). Fortunately, none of these artifacts lie near the giant arc, which is the focus of our current work.

4. Highly Magnified Star(s) at $z \simeq 4.8$

The JWST imaging of the giant arc ($z \simeq 4.8$) hosting the two star candidates is marked by a white dashed box in Figure 1. The same giant arc in the six different NIRCcam filters is shown in Figure 2. In each image, we show the position of the lensed star candidates, *star-1* and *star-2*, by the green and red arrows, respectively. A color image of the same arc is shown in Figure 3. In the color image, the positions of *star-1* and *star-2*, (R.A., decl.) = ($6^{\text{hr}}48^{\text{m}}00^{\text{s}}.3732$, $+70^{\circ}14'57''$ 948) and ($6^{\text{hr}}48^{\text{m}}00^{\text{s}}.3320$, $+70^{\circ}14'57''$ 761), respectively, are shown by green and white stars. The photometry of *star-1* and *star-2* are shown in Table 1.

4.1. Macro-magnification

To determine the position of the macro-critical curve independently of the lens models, we use a pair of strongly lensed, multiply imaged clumps in the arc, which are situated at the edges of the white lines drawn along the arc in Figure 3. Using the ratio of the distances between the two clumps on each side of the critical curve (i.e., the distance between 2.1a and 2.1b divided by the distance between 2.2a and 2.2b), and the distance between the counter-images of the innermost clump (i.e., distance between 2.1a and 2.2a), the position of the macro-critical curve can be estimated and is shown by the yellow dashed line drawn perpendicular to the arc.³⁹ The critical curves predicted that way, although only a first-order approximation, are consistent with the lens models, offering greater confidence that these objects lie very near to the critical

³⁸ referred to as “Zitrin-Analytic” in some of these studies.

³⁹ One can also use the flux ratios of counter-images of strongly lensed clumps to estimate the critical curve position independently.

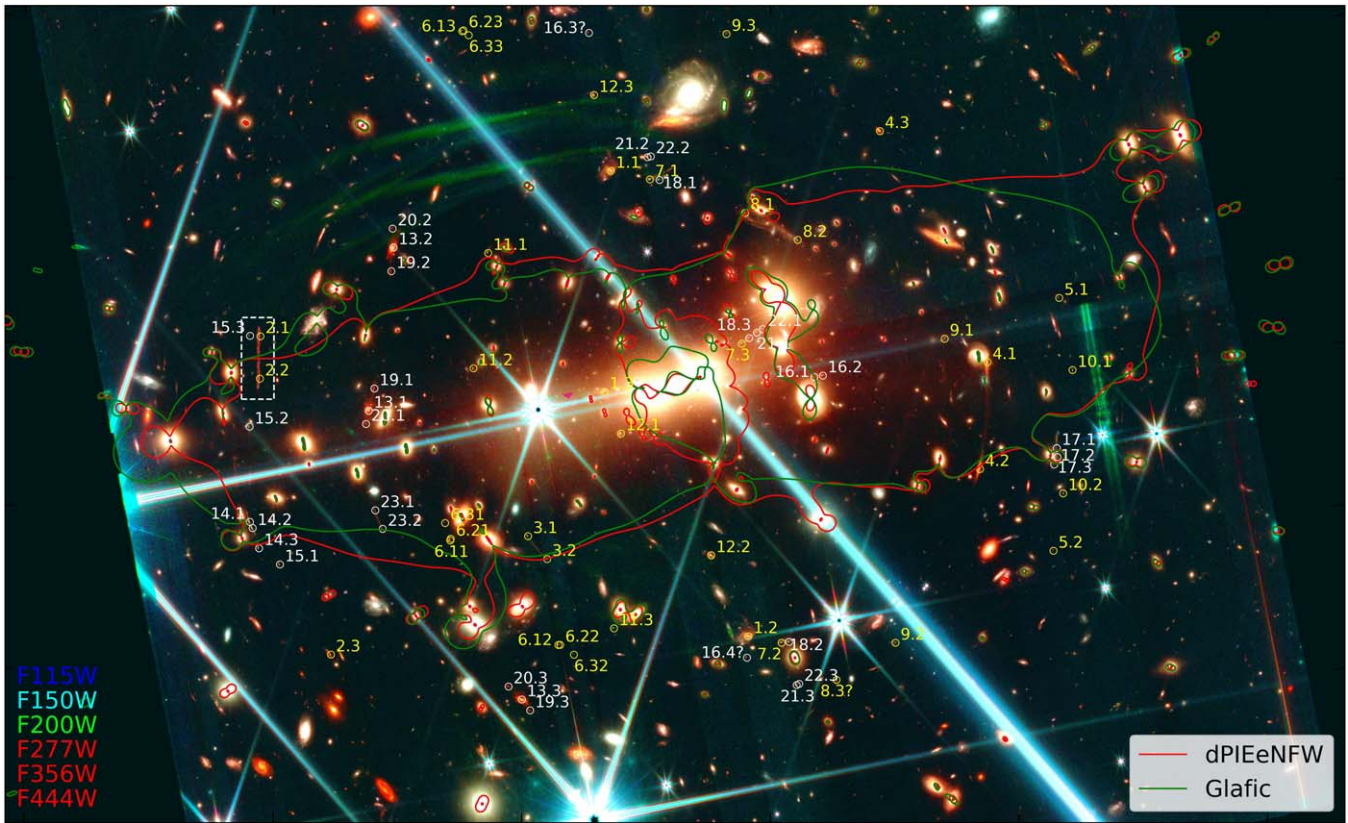


Figure 1. JWST/NIRCam false color image ($R = F277W + F356W + F444W$; $G = F150W + F200W$; $B = F115W + F150W$) of MACS0647. Multiple images are indicated and numbered. The yellow circles mark lensed image systems previously identified in HST observations, and the white circles denote lensed systems newly identified with JWST. The red and green curves represent the macro-critical curves corresponding to our dPIEeNFW and Glafic lens models, respectively, for a source at redshift $z_s = 4.8$. The white dashed box marks the position of the “giant arc” (resulting from the merger of images 2.1 and 2.2) in which the lensed star candidates are detected. The panel size is $2''.73 \times 1''.64$ across.

Table 1
Photometry of star-1 and star-2

Filter (1)	star-1 (2)	star-2 (3)
F115W	29.351 ± 0.604	29.786 ± 0.823
F150W	29.028 ± 0.600	29.921 ± 0.721
F200W	28.311 ± 0.241	28.746 ± 0.301
F277W	27.343 ± 0.199	28.330 ± 0.378
F356W	27.795 ± 0.244	29.059 ± 0.471
F444W	27.996 ± 0.327	29.406 ± 0.666

Note. Column 1: JWST filter name; Columns 2 and 3: measured apparent magnitudes of star-1 and star-2 with 1σ error bars.

curves. According to this model-independent estimation of the critical curve, both star-1 and star-2 are situated on the saddle side, at distances of $<0''.1$ and $\sim 0''.32$, respectively, from the macro-critical curve. According to our dPIEeNFW model, star-1 sits “on” (i.e., within \sim half the spatial resolution limit from) the macro-critical curve, whereas star-2 lies at a distance of $\sim 0''.18$ from the macro-critical curve. The Glafic model gives distances of $\sim 0''.25$ and $\sim 0''.50$ for star-1 and star-2 from the macro-critical curve, respectively. The macro-magnification ($|\mu|$) value at the position of star-1 (star-2) is ~ 600 (~ 90) and ~ 190 (~ 50) according to the dPIEeNFW and Glafic lens models, respectively.

4.2. Photometry

To measure the photometry of the lensed star candidates, we follow a procedure similar to that described in Welch et al. (2022b). For each one of the filters, pixels associated with the star are identified using the clumps segmentation map provided by NoiseChisel and Segment (Akhlaghi & Ichikawa 2015). It is important to note that we run Segment, disabling any kernel convolution, to identify better the pixels that correspond to the star, thus avoiding any artificial extension of the region due to smoothing. We call these pixels “the star region”. Then, we interpolate everything that surrounds the lensed star (the arc, the light from nearby galaxies, the intracluster light, and the sky) iteratively, using the interpolation algorithm included in the pipeline CICLE (Jiménez-Teja et al. 2018). This algorithm places apertures in the star region and its surroundings randomly. If an aperture is not fully contained in the star region, its pixels are substituted by the median of the values outside the star region. Repeating this process iteratively, we cover the entire star region with apertures, interpolating all the pixels outside-in. The flux of the star is measured by subtracting the interpolated image from the original one, in a circular aperture of radius $0''.3$. This approach has the advantage of minimizing the impact of a potential misestimation of the sky in the final photometry since this is the difference of two images, where this term cancels out. Because the apertures of the interpolation are placed randomly, we can get different values of the flux of the star in different realizations. We thus run the interpolation algorithm

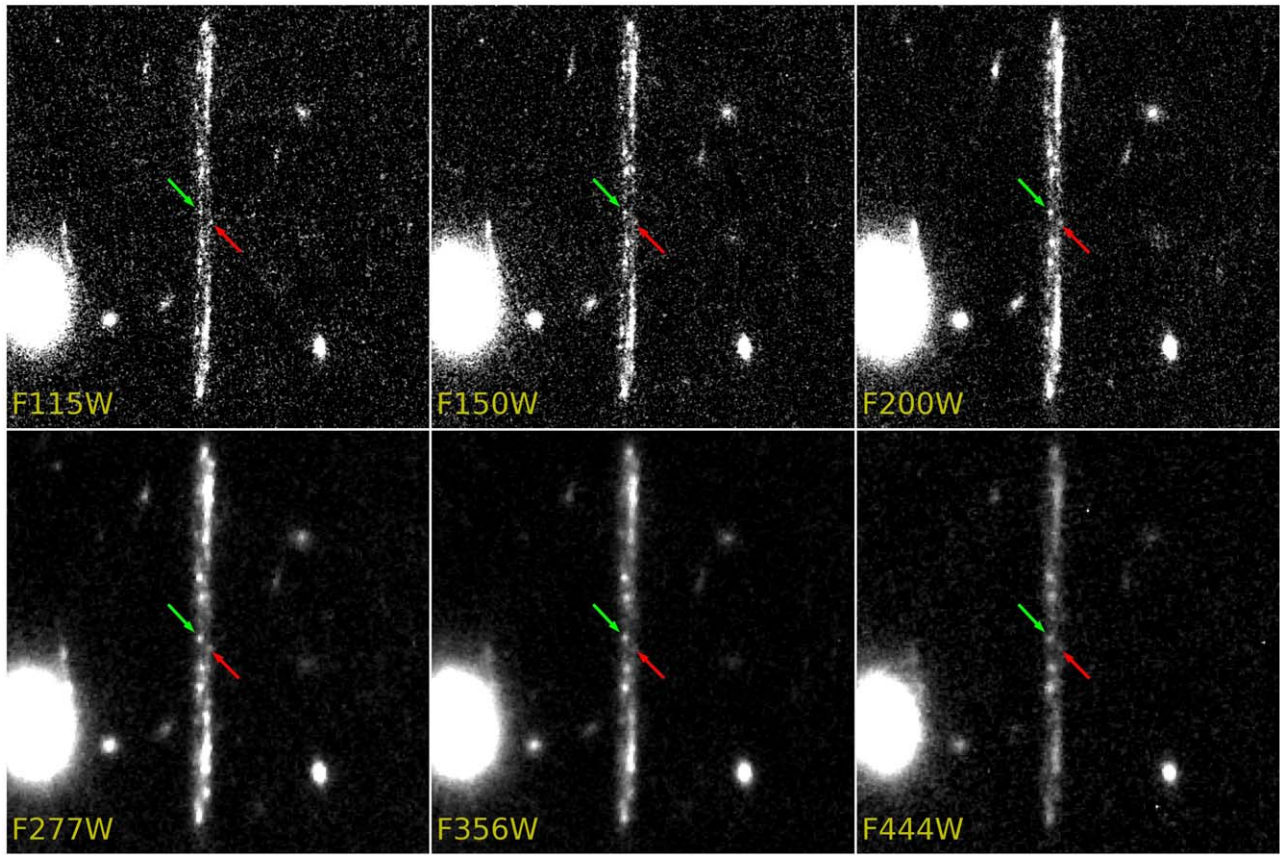


Figure 2. The two lensed star candidates in different JWST filters. In each panel, the positions of *star-1* and *star-2* on the lensed arc are shown by green and red arrows, respectively. Each panel is $8''.4 \times 8''.4$ across.

100 times for each filter, and the standard deviation of the 100 measurements is included in the error budget along with the photometric error. Finally, the fluxes are corrected for the encircled energy.

4.3. Comparison with Stellar Models

The photometry of *star-1* and *star-2* are shown by solid black points in the middle and bottom panels of Figure 4, respectively. The top panel shows the relevant filter response curves. For each candidate, we present stellar spectral energy distributions (SEDs) based on the Lejeune et al. (1997) set of stellar atmosphere spectra for three different effective temperatures (T_{eff}), which all provide acceptable fits to the data given the error bars (blue, green, and red lines, with the green line indicating the best fit). While the details of stellar atmosphere spectra depend on additional parameters such as metallicity and surface gravity, the coarse sampling of our photometric data points in practice only allows us to constrain T_{eff} (determined by the relative shape of the SED) and μL (which determines the absolute scaling required to match the observed fluxes). Throughout this fitting exercise, we treat these as independent parameters. In the SED fits plotted, we have adopted stellar atmosphere spectra with a metallicity of $[M/H] = -1$ and a surface gravity in the range $\log(g) = 2-2.5$, under the assumption that the redshift is $z = 4.8$ and that the observed SED is unaffected by dust reddening. From the plot, we can see that a star with a temperature of $T_{\text{eff}} \sim 9000-10,000$ K, i.e., in the transition from A- to B-type stars, provides a good fit to the observed photometry of *star-1*, whereas a star with $\sim 12,000$ K provides a reasonable fit for *star-2*, albeit

which a more uncertain T_{eff} due to the significantly larger photometric errors. While the fits are relatively insensitive to the assumed metallicity, corrections for reddening due to circumstellar dust, or dust within the host galaxy of the star would shift both the inferred T_{eff} and luminosity to higher values. When the μL estimates from Figure 4 are combined with the macro-magnifications derived from the dPIEeNFW and Glafic lens models, it appears that $\log(L/L_{\odot})$ could be as high as 6.7–7.5 and 7.0–7.6 for the two stars, respectively, suggesting that they may be evolved, extremely massive stars with initial masses in the 300–600 M_{\odot} range (e.g., Szecsi et al. 2022). However, the magnification of each star could be significantly enhanced by microlensing by stars in the lensing cluster, which would significantly reduce the required intrinsic luminosities and stellar masses of these objects. Indeed, at temperatures of $T_{\text{eff}} \sim 10,000$ K, stars with $\log(L/L_{\odot}) > 5.5-6$ would be in tension with the Humphreys–Davidson limit (Humphreys & Davidson 1979), an empirical luminosity limit above which almost no stars with $T_{\text{eff}} \lesssim 15,000$ K are known in the local universe.

To set a rough lower limit on the initial masses of stars that potentially could attain sufficient microlensing magnifications to match the observed fluxes of *star-1* and *star-2*, we need to consider the likely sizes of these stars. Supergiants in the $T_{\text{eff}} \sim 10,000$ K range can easily reach radii of several hundred R_{\odot} , and this limits the peak microlensing magnification that one can expect. To estimate the peak magnification for *star-1* we assume it lies essentially on the critical curve (i.e., within the corrugated microcaustic network), as suggested by our dPIEeNFW lens model. We then use Equation (27) from

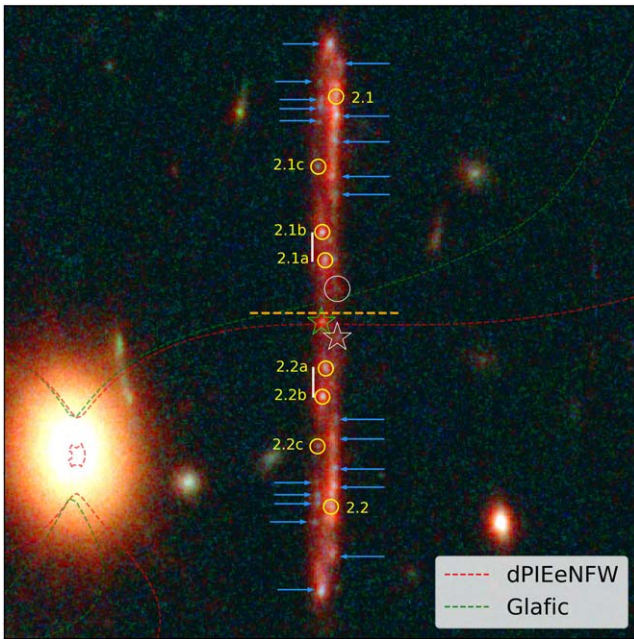


Figure 3. Highly magnified star candidates in the strongly lensed arc at $z_s = 4.8$. The dashed red and green curves represent the critical curve corresponding to the dPIEeNFW and Glafic lens mass models, respectively. The positions of star-1 and star-2 are marked by the green and white stars, respectively. The dashed yellow line perpendicular the arc shows the position of the macro-critical curve on the arc estimated model-independently using the distances between the counter-images of two strongly lensed knots. These knots sit at the endpoints of the white lines drawn along the arc. The blue arrows show various multiply imaged clumps in the galaxy. The yellow-circled clumps are the only one used in the dPIEeNFW lens model reconstruction. The white circle marks the position of a fainter, possible counter-image of star-2. The panel is $8''.4 \times 8''.4$ across.

Venumadhav et al. (2017), which specifies the peak magnification in the corrugated network. Using the relevant lensing parameters, such as a convergence value ($\kappa = 0.55$) and the modulus of the gradient of $\kappa + \gamma$ (Venumadhav et al. 2017), we obtain that the typical peak magnification at the position of star-1 is $\sim [10^5, 10^4] \times (R/10 R_\odot)^{-1/2}$ for a source with radius R . Here we assumed that microlenses at the candidate position can contribute in the range [0.1%, 1%] of the total surface density (Σ_{tot}) with a microlens mass of $1 M_\odot$. In Figure 5, we use the peak magnification–star radius relation to demonstrate that stellar evolutionary tracks which predict high-mass stars reaching temperatures of $T_{\text{eff}} \approx 10,000$ K during late stages of evolution suggest that a subset of such stars ($\sim 20\text{--}100 M_\odot$ for the models plotted) are sufficiently compact to be extremely magnified and observed by us. As mentioned in the Introduction, so far, nearly all galaxy clusters observed with JWST have led to the detection of lensed stars. In addition, as shown in Welch et al. (2022a) for “Earendel,” the probability of detecting massive lensed stars ($M \sim 100 M_\odot$) is roughly 1 in every 25–50 lensed arcs depending on various parameters. Our lensed star candidate lies at a somewhat smaller redshift and has an allowed mass range [$\sim 20\text{--}100 M_\odot$], implying that the above number can be used as a lower limit. Apart from that, we note that the microlens density values similar to $0.1 \times \Sigma_{\text{tot}}$ might be unlikely to occur. But we should keep in mind that we are only estimating the average peak magnification, and we can still get higher (or lower) peak values than the average value. Hence, we may get peaks equivalent to the average peak value corresponding to

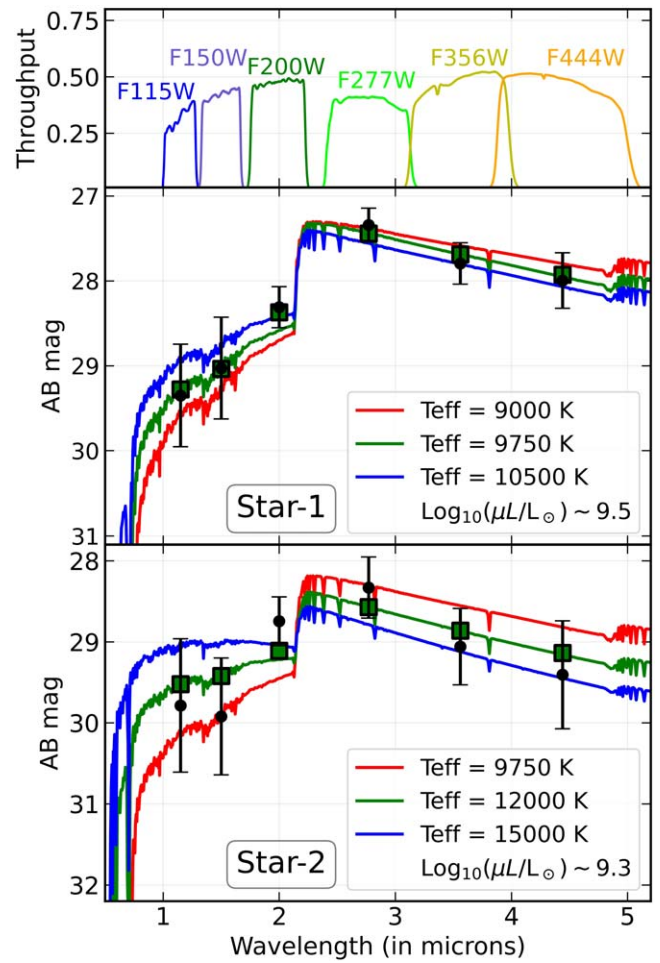


Figure 4. Measured photometry of star-1 and star-2 and the corresponding SED model fits are shown in middle and bottom panels, respectively. The black solid points with error bars represent the observed AB magnitudes and their 1σ errors, respectively, for the lensed star candidates, in the various JWST/NIRCam filters. The red, green, and blue curves for each candidate represent three acceptable single-star SED fits, with the green SED being the best-fitting one. For the green SEDs, we also plot the integrated broadband fluxes (filled squares) resulting from the model and present the best-fitting $\log(\mu L/L_\odot)$ scaling of this fit. The filter throughput curves are shown on the top panel.

$0.1 \times \Sigma_{\text{tot}}$ even for somewhat larger values of the microlens density.

As for star-2, we find it most likely lies farther away from the macro-caustic and outside the corrugated network, whose expected size is $\lesssim 100$ mas. At the position of star-2, the typical peak magnification is thus estimated using Equation (26) from Oguri et al. (2018), which describes the peak magnification outside the corrugated network, i.e., in the low optical depth regime where it is assumed that the peak is due to a single microlens caustic crossing. With this, we find $\sim 10^4 (R/10 R_\odot)^{-1/2}$, for which we can use the red line shown in Figure 5 to estimate what type of stars can get bright enough to be observed. We find that the preferable mass for star-2 is $\gtrsim 50 M_\odot$.

4.4. What if Not Lensed Stars?

One interesting possibility we should also consider is that the candidates are lensed star clusters instead of individual stars. Since the stars are unresolved, i.e., if we adopt a point-spread

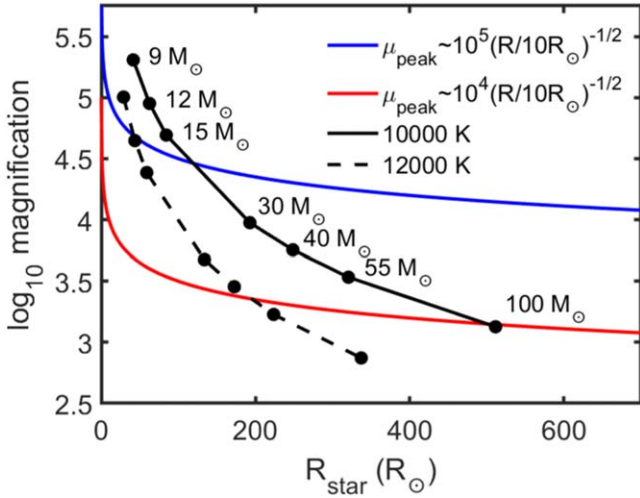


Figure 5. Radius–magnification limits for highly magnified stars. The red and blue lines represent the peak magnifications reached by microcaustic crossings as a function of the star’s radius (Venumadhav et al. 2017; Oguri et al. 2018), for the two scenarios implied by the locations of *star-1* and *star-2*, respectively. The filled black circles along the solid and dashed black lines indicate the relation between stellar radius, for the $T_{\text{eff}} \approx 10,000$ K (*star-1*) and $T_{\text{eff}} \approx 12,000$ K (*star-2*) models of different initial mass from the BoOST (Szecsi et al. 2022) SMC-metallicity stellar evolutionary tracks, and the magnification required for these to match the apparent brightness of the two candidates. For *star-1*, only stellar models with initial masses $\gtrsim 20 M_{\odot}$ on the solid black line fall below the blue radius–magnification line, and are thus considered plausible, whereas stars smaller than this mass limit fall above the blue line, indicating they require too large magnifications for their predicted sizes. Similarly, for *star-2* only stars with masses $\gtrsim 50 M_{\odot}$ on the dashed black line fall below the red line and remain viable candidates. In the case of the stellar evolutionary tracks used here, stars with initial masses above $100 M_{\odot}$ never reach temperatures as low as those inferred by the SED fits to our two candidates.

function FWHM of $0''.03$ as their maximum size, and assuming a tangential magnification of 500 taken from the dPIEeNFW model at the position of *star-1*, the upper limit on the rest-frame size of the source is <0.38 pc, making a star cluster less likely. For *star-2*, which lies farther from the critical curve, we would expect a similarly magnified counter-image, if it is a star cluster. As shown in Figure 3, we do observe a possible counter-image of *star-2* on the other side of the macro-critical curve. However, this possible counter-image is noticeably fainter compared to the *star-2*, and so it is unclear if it is indeed a counter-image. If this is a counter-image, and *star-2* is a star cluster, the flux anomaly might be explained, for example, in one of the following ways: (1) the saddle-side image which we dubbed *star-2*, gets an additional magnification boost due to the presence of a subhalo near its position, making it brighter; or (2) one or more of the stars in the star cluster on the saddle-side image is going through a microlensing event, making the saddle-side image brighter than the minima-side image. Future observations will help determine the nature of these sources. We refer the reader also to Welch et al. (2022a, 2022b) for additional information regarding the lensing of star clusters versus stars.

The original selection for the star candidates here was based on their compact size, proximity to the critical curves, symmetry arguments (in particular, a lack of counter-images), and supported further by their SED fits. Nevertheless, other possible explanations should be acknowledged. We discuss here whether these may be small persistent objects at the

Table 2
Multiple-image Systems in MACS0647

ID (1)	R.A. (2)	Decl. (3)	z_{phot} (4)	Comments (5)
1.1	101.9660445	70.2558166	$2.13^{+0.33}_{-0.18}$	Zitrin et al. (2011)
1.2	101.9522096	70.2399951	$1.85^{+0.55}_{-0.02}$...
1.3	101.9666816	70.2483074
2.1	102.0013086	70.2501887	$4.76^{+0.07}_{-0.16}$	Zitrin et al. (2011)
2.2	102.0013546	70.2487492	$4.79^{+0.07}_{-0.15}$...
2.3	101.9941933	70.2393721	$4.72^{+0.13}_{-0.16}$...
3.1	101.9743730	70.2433988	$3.32^{+0.08}_{-0.10}$	Coe et al. (2013)
3.2	101.9724519	70.2426198	$2.78^{+0.49}_{-0.04}$...
4.1	101.9281515	70.2493187	$2.46^{+0.04}_{-1.34}$	Coe et al. (2013)
4.2	101.9289077	70.2456830	$1.86^{+0.66}_{-0.03}$...
4.3	101.9389774	70.2571705	$2.05^{+0.41}_{-0.27}$...
5.1	101.9209434	70.2514986	$6.33^{+0.32}_{-0.26}$	Coe et al. (2013)
5.2	101.9215289	70.2429026	$6.91^{+0.37}_{-0.53}$...
6.11	101.9821971	70.2432514	$10.62^{+0.27}_{-0.21}$	Coe et al. (2013)
6.12	101.9713212	70.2397022	$10.58^{+0.32}_{-0.37}$...
6.13	101.9810192	70.2605628	$10.22^{+0.50}_{-0.62}$...
6.21	101.9821500	70.2433072	...	Hsiao & Coe (2022)
6.22	101.9711412	70.2397047
6.23	101.9808954	70.2605925
6.31	101.9827102	70.2438447	$0.52^{+9.67}_{-0.06}$	Hsiao & Coe (2022)
6.32	101.9697561	70.2393690	$9.19^{+1.12}_{-6.97}$...
6.33	101.9803691	70.2604279	$10.62^{+0.92}_{-0.86}$...
7.1	101.9621250	70.2555278	$2.04^{+0.18}_{-0.19}$	Coe et al. (2013)
7.2	101.9488750	70.2397778
7.3	101.9528750	70.2499444	$2.15^{+0.17}_{-0.09}$...
8.1	101.9525417	70.2543889	$2.45^{+0.08}_{-0.29}$	Coe et al. (2013)
8.2	101.9472500	70.2534722	$2.31^{+0.12}_{-0.24}$...
8.3?	101.9433492	70.2385144	$2.37^{+0.23}_{-0.30}$...
9.1	101.9324583	70.2501111	$5.74^{+0.27}_{-0.24}$	Coe et al. (2013)
9.2	101.9374167	70.2397778	$5.77^{+0.40}_{-0.16}$...
9.3	101.9544167	70.2604722	$5.94^{+0.29}_{-0.26}$...
10.1	101.9196004	70.2490478	$7.34^{+0.36}_{-0.16}$	Zitrin et al. (2015)
10.2	101.9205483	70.2448550	$7.33^{+0.31}_{-0.11}$...
11.1	101.9783943	70.2530223	$1.98^{+0.69}_{-0.22}$	Zitrin et al. (2015)
11.2	101.9798736	70.2491041
11.3	101.9657264	70.2402669
12.1	101.9650223	70.2468672	$2.22^{+0.19}_{-0.20}$	Zitrin et al. (2015)
12.2	101.9559227	70.2427413	$2.45^{+0.06}_{-0.20}$...
12.3	101.9677194	70.2583876	$2.14^{+0.30}_{-0.13}$...
13.1	101.9904001	70.2476587	$3.53^{+0.21}_{-0.07}$	New system
13.2	101.9879212	70.2532128	$3.50^{+0.24}_{-0.04}$...
13.3	101.9749885	70.2378465	$3.50^{+0.25}_{-0.04}$...
14.1	102.0023538	70.2438789	$2.86^{+0.36}_{-0.12}$	New system
14.2	102.0020778	70.2436712	$3.21^{+0.09}_{-0.20}$...
14.3	102.0014310	70.2429844	$3.24^{+0.15}_{-3.03}$...
15.1	101.9993248	70.2424316	$11.40^{+0.21}_{-0.25}$	New system
15.2	102.0023951	70.2471152	$0.39^{+0.19}_{-0.09}$...
15.3	102.0023503	70.2502045	$3.38^{+0.33}_{-0.25}$...
16.1	101.9455802	70.2488149	...	New system
16.2	101.9447169	70.2488604	$6.69^{+0.05}_{-2.20}$...
16.3?	101.9682583	70.2605087	$6.71^{+0.12}_{-0.11}$...
16.4?	101.9523528	70.2392696	$6.70^{+0.08}_{-0.07}$...
17.1	101.9211918	70.2463921	$2.46^{+0.18}_{-0.32}$	New system
17.2	101.9211231	70.2460865
17.3	101.9214513	70.2458354
18.1	101.9611602	70.2555089	$2.14^{+0.03}_{-0.03}$	New system
18.2	101.9481108	70.2398067
18.3	101.9521371	70.2501341	$2.15^{+0.02}_{-0.04}$...

Table 2
(Continued)

ID (1)	R.A. (2)	Decl. (3)	z_{phot} (4)	Comments (5)
19.1	101.9898364	70.2484166	$3.73^{+0.53}_{-0.73}$	New system
19.2	101.9881425	70.2524040	$3.60^{+0.45}_{-0.55}$...
19.3	101.9741549	70.2374749	$3.54^{+0.42}_{-0.47}$...
20.1	101.9906731	70.2472096	$3.76^{+0.60}_{-2.78}$	New system
20.2	101.9880141	70.2538524	$3.39^{+0.22}_{-0.12}$...
20.3	101.9763250	70.2382859	$3.31^{+0.42}_{-1.52}$...
21.1	101.9513568	70.2503220	$2.86^{+0.22}_{-0.18}$	New system
21.2	101.9623645	70.2562833	$2.73^{+0.32}_{-0.12}$...
21.3	101.9473538	70.2383398	$2.86^{+0.26}_{-0.18}$...
22.1	101.9507687	70.2504387	$3.02^{+0.15}_{-0.35}$	New system
22.2	101.9620375	70.2563121
22.3	101.9471011	70.2383789
23.1	101.9897367	70.2442761	$3.05^{+0.66}_{-0.27}$	New system
23.2	101.9890000	70.2436439	$2.74^{+0.42}_{-1.94}$...

Note. Column 1: Lens system ID; Columns 2 & 3: R.A. and decl.; Column 4: EAZY (Brammer et al. 2008) photometric redshift with 95% confidence interval estimated using HST and JWST observations; Column 5: system reference.

redshift of the cluster, or at other low redshifts; or some transient phenomena, in the cluster, or at the source. The break near $\sim 2.1 \mu\text{m}$ in the measured SEDs of the candidates, seen in Figure 4, matches very well the rest-frame Balmer break of A/B-stars at a redshift of 4.8 (rest-frame wavelength of $\sim 0.3646 \mu\text{m}$). Owing to this break, the possibility that the candidates are interlopers at lower redshift or in the galaxy cluster—such as compact galaxies, star clusters, or even transient phenomena such as supernovae—seems unlikely, because we do not expect a break at $\sim 2.1 \mu\text{m}$ for typical objects at the cluster’s redshift. We note that (as mentioned above) in Figure 4, presence of the Balmer break for *star-1* is convincing whereas for *star-2* it is not due to the large error bars.

Transient phenomena in the source galaxy, which in principle should be pondered as well given the lack of counter-images, also seem unlikely: the expected observed time-delay between the observed candidates and their expected counter-images on the outer side of the macro-critical curve is $< +0.42$ days, where the “+” sign indicates that the observed candidates are trailing images so that images outside the macro-critical curve should have appeared up to a few hours before. Hence, only optical transients that last less than a few hours are possible candidates. If the candidates were some type of stellar explosions such as (kilo)novae or supernovae, we should have also detected their counter-images. The non-detection of counter-images on the outer side of the macro-critical curve thus allows us to discard any transient lasting more than 0.42 days in the observe frame. This also includes a stellar-mass black hole accreting mass from an asymptotic giant branch (AGB) companion (see Windhorst et al. 2018) as such objects are not expected to show the observed break, and their timescales should be longer.

5. Conclusions

In this work, we report two highly magnified lensed star candidates detected in the JWST/NIRCam imaging of MACS0647 acquired through the JWST cycle 1 GO

program (program ID: 1433; PI: Dan Coe). These candidates were observed in a giant arc at a redshift of $z_{\text{phot}} \simeq 4.8$, making them the second farthest lensed star candidates after “Earendel” ($z \simeq 6.2$; Welch et al. 2022a, 2022b) known to date. From a combination of magnification constraints and SED fitting, the estimated temperatures for the two stars are $\sim 10,000$ K and $\sim 12,000$ K, respectively. Using stellar evolutionary tracks, we find that stars with masses $\gtrsim 20 M_{\odot}$ and $\gtrsim 50 M_{\odot}$ are viable candidates for *star-1* and *star-2*, respectively, assuming peak magnifications inferred from the analytical relations given in Venumadhav et al. (2017) and Oguri et al. (2018), appropriate for our cases.

Based on the SED fits, lensing arguments—including magnification, or proximity to the critical curves, symmetry, and time-delay—along with the absence of counter-images, we suggest that *star-1* is very likely a lensed star. For *star-2*, we observe a possible, faint counter-image on the minima-side of the macro-critical curve, which—if true—may suggest it is instead a star cluster. In such a case the flux ratio anomaly between the star cluster and its expected counter-image would need to be explained, possibly by micro or milli-lensing at its observed position. Some other possible objects are also considered and deemed here unlikely, although it should be acknowledged that there may be other fitting, known or unknown, of different types of interlopers not considered here.

Assuming that the candidates are indeed lensed stars (or star complexes), we can expect that future observations would show variations in their light curves on timescales of hours to days, depending on the size of the source and relative velocity between the lens and source. The sizes of the fluctuations are determined mainly by the distance from the caustic, size of the star, and underlying macro model parameters. Planned spectroscopic observations in early 2023 will help us further deduce the nature of these candidates.

A.K.M., A.Z., and L.J.F. acknowledge support from grant 2020750 from the United States-Israel Binational Science Foundation (BSF) and grant 2109066 from the United States National Science Foundation (NSF), and by the Ministry of Science & Technology, Israel. Y.J.-T. acknowledges financial support from the European Union’s Horizon 2020 research and innovation program under the Marie Skłodowska-Curie grant agreement No. 898633, the MSCA IF Extensions Program of the Spanish National Research Council (CSIC), and the State Agency for Research of the Spanish MCIU through the Center of Excellence Severo Ochoa award to the Instituto de Astrofísica de Andalucía (SEV-2017-0709). E.Z. acknowledges funding from the Swedish National Space Agency. J.M. D. acknowledges the support of projects PGC2018-101814-B-100 and MDM-2017-0765. B.W. acknowledges support from NASA under award No. 80GSFC21M0002. A.A. acknowledges support from the Swedish Research Council (Vetenskapsrådet project grants 2021–05559). R.A.B gratefully acknowledges support from the European Space Agency (ESA) Research Fellowship. M.B. acknowledges support from the Slovenian national research agency ARRS through grant N1-0238. P.D. acknowledges support from the NWO grant 016.VIDI.189.162 (“ODIN”) and from the European Commission’s and University of Groningen’s CO-FUND Rosalind Franklin program. G.M. acknowledges funding from the European Union’s Horizon 2020 research and innovation program under the Marie Skłodowska-Curie grant

agreement No. MARACHAS—DLV-896778. R.A.W. acknowledges support from NASA JWST Interdisciplinary Scientist grants NAG5-12460, NNX14AN10G and 80NSSC18K0200 from GSFC.

Facilities: JWST(NIRCam), HST(ACS, WFC3).

Software: Python (<https://www.python.org>), NumPy~ (Harris et al. 2020), AstroPy (Price-Whelan et al. 2018), Matplotlib (Hunter 2007), GRIZLI (Brammer et al. 2022), EAZY (Brammer et al. 2008), Glafic (Oguri 2010), dPIEeNFW (Zitrin et al. 2015).

ORCID iDs

Ashish Kumar Meena  <https://orcid.org/0000-0002-7876-4321>

Adi Zitrin  <https://orcid.org/0000-0002-0350-4488>

Yolanda Jiménez-Teja  <https://orcid.org/0000-0002-6090-2853>

Erik Zackrisson  <https://orcid.org/0000-0003-1096-2636>

Wenlei Chen  <https://orcid.org/0000-0003-1060-0723>

Dan Coe  <https://orcid.org/0000-0001-7410-7669>

Jose M. Diego  <https://orcid.org/0000-0001-9065-3926>

Paola Dimauro  <https://orcid.org/0000-0001-7399-2854>

Lukas J. Furtak  <https://orcid.org/0000-0001-6278-032X>

Patrick L. Kelly  <https://orcid.org/0000-0003-3142-997X>

Masamune Oguri  <https://orcid.org/0000-0003-3484-399X>

Brian Welch  <https://orcid.org/0000-0003-1815-0114>

Abdurro'uf  <https://orcid.org/0000-0002-5258-8761>

Felipe Andrade-Santos  <https://orcid.org/0000-0002-8144-9285>

Angela Adamo  <https://orcid.org/0000-0002-8192-8091>

Rachana Bhatawdekar  <https://orcid.org/0000-0003-0883-2226>

Maruša Bradač  <https://orcid.org/0000-0001-5984-0395>

Larry D. Bradley  <https://orcid.org/0000-0002-7908-9284>

Tom Broadhurst  <https://orcid.org/0000-0002-8785-8979>

Christopher J. Conselice  <https://orcid.org/0000-0003-1949-7638>

Pratika Dayal  <https://orcid.org/0000-0001-8460-1564>

Megan Donahue  <https://orcid.org/0000-0002-2808-0853>


Brenda L. Frye  <https://orcid.org/0000-0003-1625-8009>

Seiji Fujimoto  <https://orcid.org/0000-0001-7201-5066>

Tiger Yu-Yang Hsiao  <https://orcid.org/0000-0003-4512-8705>

Vasily Kokorev  <https://orcid.org/0000-0002-5588-9156>

Guillaume Mahler  <https://orcid.org/0000-0003-3266-2001>

Eros Vanzella  <https://orcid.org/0000-0002-5057-135X>

Rogier A. Windhorst  <https://orcid.org/0000-0001-8156-6281>

References

Adams, N. J., Conselice, C. J., Ferreira, L., et al. 2023, *MNRAS*, 518, 4755
Akhlaghi, M., & Ichikawa, T. 2015, *ApJS*, 220, 1

Astropy Collaboration, Price-Whelan, A. M., Sipőcz, B. M., et al. 2018, *AJ*, 156, 123
Atek, H., Shuntov, M., Furtak, L. J., et al. 2023, *MNRAS*, 519, 1201
Bhatawdekar, R., Conselice, C. J., Margalef-Bentabol, B., & Duncan, K. 2019, *MNRAS*, 486, 3805
Brammer, G., Strait, V., Matharu, J., & Momcheva, I. 2022, *grizli*, v1.5.0, Zenodo, doi:10.5281/zenodo.6672538
Brammer, G. B., van Dokkum, P. G., & Coppi, P. 2008, *ApJ*, 686, 1503
Castellano, M., Fontana, A., Treu, T., et al. 2022, *ApJL*, 938, L15
Chan, B. M. Y., Broadhurst, T., Lim, J., et al. 2017, *ApJ*, 835, 44
Chen, W., Kelly, P. L., Diego, J. M., et al. 2019, *ApJ*, 881, 8
Chen, W., Kelly, P. L., Treu, T., et al. 2022, *ApJL*, 940, L54
Coe, D., Fuselier, E., Benítez, N., et al. 2008, *ApJ*, 681, 814
Coe, D., Zitrin, A., Carrasco, M., et al. 2013, *ApJ*, 762, 32
Diego, J. M. 2019, *A&A*, 625, A84
Diego, J. M., Pascale, M., Kavanagh, B. J., et al. 2022a, *A&A*, 665, A134
Diego, J. M., Kaiser, N., Broadhurst, T., et al. 2018, *ApJ*, 857, 25
Diego, J. M., Meena, A. K., Adams, N. J., et al. 2022b, arXiv:2210.06514
Ebeling, H., Barrett, E., Donovan, D., et al. 2007, *ApJL*, 661, L33
Furtak, L. J., Shuntov, M., Atek, H., et al. 2023, *MNRAS*, 519, 3064
Gardner, J. P., Mather, J. C., Clampin, M., et al. 2006, *SSRv*, 123, 485
Harris, C. R., Millman, K. J., van der Walt, S. J., et al. 2020, *Natur*, 585, 357
Hsiao, T. Y.-Y., & Coe, D. 2022, arXiv:2210.14123
Humphreys, R. M., & Davidson, K. 1979, *ApJ*, 232, 409
Hunter, J. D. 2007, *CSE*, 9, 90
Jiménez-Teja, Y., Dupke, R., Benítez, N., et al. 2018, *ApJ*, 857, 79
Jullo, E., Kneib, J. P., Limousin, M., et al. 2007, *NJPh*, 9, 447
Kurov, A. A., Dai, L., Venumadhav, T., Miralda-Escudé, J., & Frye, B. 2019, *ApJ*, 880, 58
Keeton, C. R. 2010, *GRGr*, 42, 2151
Kelly, P. L., Chen, W., Alfred, A., et al. 2022, arXiv:2211.02670
Kelly, P. L., Diego, J. M., Rodney, S., et al. 2018, *NatAs*, 2, 334
Kelly, P. L., Rodney, S. A., Treu, T., et al. 2016, *ApJL*, 819, L8
Kneib, J. P., Mellier, Y., Fort, B., & Mathez, G. 1993, *A&A*, 273, 367
Lejeune, T., Cuisinier, F., & Buser, R. 1997, *A&AS*, 125, 229
Meena, A. K., Arad, O., & Zitrin, A. 2022a, *MNRAS*, 514, 2545
Meena, A. K., Chen, W., Zitrin, A., et al. 2022b, arXiv:2211.01402
Meneghetti, M., Natarajan, P., Coe, D., et al. 2017, *MNRAS*, 472, 3177
Miralda-Escudé, J. 1991, *ApJ*, 379, 94
Navarro, J. F., Frenk, C. S., & White, S. D. M. 1996, *ApJ*, 462, 563
Oguri, M. 2010, *PASJ*, 62, 1017
Oguri, M., Diego, J. M., Kaiser, N., Kelly, P. L., & Broadhurst, T. 2018, *PhRvD*, 97, 023518
Okabe, T., Oguri, M., Peirani, S., et al. 2020, *MNRAS*, 496, 2591
Oke, J. B., & Gunn, J. E. 1983, *ApJ*, 266, 713
Pascale, M., Frye, B. L., Diego, J., et al. 2022, *ApJL*, 938, L6
Postman, M., Coe, D., Benítez, N., et al. 2012, *ApJS*, 199, 25
Roberts-Borsani, G., Treu, T., Chen, W., et al. 2022, arXiv:2210.15639
Rodney, S. A., Balestra, I., Bradac, M., et al. 2018, *NatAs*, 2, 324
Salmon, B., Coe, D., Bradley, L., et al. 2018, *ApJL*, 864, L22
Szécsi, D., Agrawal, P., Wünsch, R., & Langer, N. 2022, *A&A*, 658, A125
Vanzella, E., Claeysens, A., Welch, B., et al. 2022, arXiv:2211.09839
Venumadhav, T., Dai, L., & Miralda-Escudé, J. 2017, *ApJ*, 850, 49
Welch, B., Coe, D., Diego, J. M., et al. 2022a, *Natur*, 603, 815
Welch, B., Coe, D., Zackrisson, E., et al. 2022b, *ApJL*, 940, L1
Williams, H., Kelly, P. L., Chen, W., et al. 2022, arXiv:2210.15699
Windhorst, R. A., Timmes, F. X., Wyithe, J. S. B., et al. 2018, *ApJS*, 234, 41
Yan, H., Ma, Z., Ling, C., et al. 2023, *ApJL*, 942, L9
Zitrin, A., Broadhurst, T., Barkana, R., Rephaeli, Y., & Benítez, N. 2011, *MNRAS*, 410, 1939
Zitrin, A., Broadhurst, T., Umetsu, K., et al. 2009, *MNRAS*, 396, 1985
Zitrin, A., Fabris, A., Merten, J., et al. 2015, *ApJ*, 801, 44